Author Manuscript

Author Manuscript

Author Manuscript

Author Manuscript

HHS Public Access

Author manuscript

IEEE Trans Radiat Plasma Med Sci. Author manuscript; available in PMC 2024 February 01.

Published in final edited form as:

IEEE Trans Radiat Plasma Med Sci. 2023 February ; 7(2): 191–202. doi:10.1109/trpms.2022.3201151.

Joint Estimation of Metal Density and Attenuation Maps with Pencil Beam XFET

Hadley DeBrosse,

Department of Radiology, University of Chicago, Chicago, IL

Talon Chandler,

Department of Radiology, University of Chicago, Chicago, IL, and is now with Chan Zuckerberg Biohub, San Francisco, CA

Ling Jian Meng [Member, IEEE],

Department of Nuclear, Plasma, and Radiological Engineering, University of Illinois Urbana-Champaign, Urbana, IL

Patrick La Rivière [Member, IEEE]

Department of Radiology, University of Chicago, Chicago, IL

Abstract

X-ray fluorescence emission tomography (XFET) is an emerging imaging modality that images the spatial distribution of metal without requiring biochemical modification or radioactivity. This work investigates the joint estimation of metal and attenuation maps with a pencil-beam XFET system that allows for direct metal measurement in the absence of attenuation. Using singular value decomposition on a simplified imaging model, we show that reconstructing metal and attenuation voxels far from the detector is an ill-conditioned problem. Using simulated data, we develop and compare two image reconstruction methods for joint estimation. The first method alternates between updating the attenuation map with a separable paraboloidal surrogates algorithm and updating the metal map with a closed-form solution. The second method performs simultaneous joint estimation with conjugate gradients based on a linearized imaging model. The alternating approach outperforms the linearized approach for iron and gold numerical phantom reconstructions. Reconstructing an $(8\ \text{cm})^3$ object containing gold concentrations of $5\ \text{mg/cm}^3$ and an unknown beam attenuation map using the alternating approach yields an accurate gold map (NRMSE = 0.19) and attenuation map (NRMSE = 0.14). This simulation demonstrates an accurate joint reconstruction of metal and attenuation maps, from emission data, without previous knowledge of any attenuation map.

Keywords

X-ray fluorescence emission tomography; XFET; XFCT; joint estimation; emission tomography

hadleys@uchicago.edu .

Author Manuscript Author Manuscript Author Manuscript Author Manuscript

I. Introduction

X-ray fluorescence tomography is an emerging class of imaging modalities used to image the spatial distribution of trace metals [1]–[4], especially high-Z metals with theranostic and biomedical applications. Platinum-based chemotherapy agents like Cisplatin are used in cancer therapy [5], and gold nanoparticles are currently under investigation for photothermal ablation therapy of superficial cancer [6], as well as for metal-mediated radiation therapy due to their radiosensitization properties [7], [8]. Imaging the spatial distribution of other lower-Z metal is of interest in earth, material, and life sciences. Although conceptually similar to emission tomography, X-ray fluorescence tomography does not rely on radioactivity of a tracer molecule. Rather, an external X-ray source stimulates metal atoms to emit characteristic X-rays, which are then imaged by energy-sensitive detectors.

We distinguish between two major approaches to metal mapping: X-ray fluorescence *computed* tomography (XFCT), and X-ray fluorescence *emission* tomography (XFET). XFCT is an emerging modality that uses a pencil beam of X-rays to stimulate fluorescence in a material [2], [9], [10]. Those rays are detected by a non-imaging energy-sensitive detector placed perpendicularly to the sample. In the absence of attenuation, the measurement gives a line integral through the metal density map of the material. XFCT uses first-generation CT acquisition, scanning the pencil beam and rotating the sample at each position to obtain a complete sinogram, which must be reconstructed to obtain an image. In contrast, XFET utilizes a slit geometry seen in Figure 1. The object is translated perpendicularly through the beam without rotation, and metal atoms along the illuminating beam will emit fluorescence isotropically. The slit encodes position information by allowing a column of pixels within the position-sensitive detector to detect fluorescence only from a specific axial segment of the beam. With this geometry, XFET allows for direct measurement of the metal without the need for tomographic image reconstruction, reducing noise amplification, albeit with loss of geometric efficiency. Although several XFCT geometries have been explored [1], [4], [9], to our knowledge, our group is the first to consider a dose-efficient pencil beam and slit aperture geometry for the direct imaging of metal and estimation of attenuation correction.

Because in the absence of attenuation XFET is a direct imaging modality with a closed-form solution, in the presence of attenuation, emission data alone can potentially be used to reconstruct the attenuation map. In this paper, we aim to build an algorithm for XFET that simultaneously estimates the metal density map and the attenuation map at the fluorescent energy, without transmission measurements or previous knowledge of an attenuation map at any energy. Reconstructing accurate metal density maps is the primary aim of XFET; we are interested in obtaining only the attenuation information needed to reconstruct accurate metal densities. Therefore, the attenuation map can be viewed as a nuisance parameter: a parameter not of immediate interest, but that must be estimated to analyze the parameter of primary interest.

Although the attenuation map is a nuisance parameter, correcting for attenuation is critical to obtain accurate metal density maps in both XFET and XFCT, especially for high

Author Manuscript Author Manuscript Author Manuscript Author Manuscript

metal densities that cause significant self-absorption. At least two attenuation maps are needed for attenuation correction: one at the beam energy and one at the energy of the emitted fluorescent rays. If there are many elements being imaged simultaneously, there are potentially many attenuation maps that are needed at various fluorescent X-ray energies. Although XFCT allows for reconstruction of the beam attenuation map through the use of simultaneous transmission measurement, it is tedious and difficult to obtain attenuation maps at the characteristic X-ray energies. Previous attempts at image reconstruction in XFCT without pre-measured fluorescent attenuation maps include correcting for uniform attenuation of known materials [9]–[11], using transmission information to correct for self-absorption [12], using iterative algorithms [13]–[15], and expressing the unknown attenuation map in terms of known quantities and the unknown element densities [16]. Similar problems arise in emission tomography, and in time-of-flight positron emission tomography (PET), attenuation sinograms can only be determined up to a constant [17]. Previous attempts at reconstructing attenuation maps with emission data include using iterative methods [18]–[21], approaches based on consistency conditions [22]–[24], and an inverted Radon transform followed by iterative refinement [25]. In PET joint estimation, several approaches have been developed to overcome the scale problem, including the use of information from scatter coincidences [26], [27], MR-based priors [28] and transmission sources [29].

In our previous work, we showed that an alternating approach that makes use of separable paraboloidal surrogates to update the attenuation map outperforms filtered backprojection (FBP) in XFCT image reconstruction [30]. However, the present work includes the first alternating approach to incorporate a closed-form solution for the metal density map. The use of a closed-form solution in this work incorporates a direct solution to half of the reconstruction problem and decreases computation time.

As discussed above, XFCT attenuation correction is an ongoing research problem with no single conventional approach. One of the iterative methods to correct for attenuation and self-absorption is conjugate gradients: Schroer used conjugate gradients for XFCT image reconstruction [13], and Shi et al. examined a nonlinear conjugate gradients with regularization and found that it outperformed both maximum likelihood expectation maximization (MLEM) and FBP algorithms [31]. Therefore, the comparison of our novel alternating approach to conjugate gradients adds a relevant and valuable comparison to XFCT attenuation correction and image reconstruction literature.

In the XFET geometry, one or more pixelated detectors are placed parallel to the beam. During measurement, fluorescent emissions probe a variety of line integrals through the attenuation map, as visualized in Figure 2, where metal along the line of illumination allows for a large number of attenuation line integrals to be measured. The metal acts as a X-ray source in an interior-source tomography problem, and its spatial distribution heavily determines what section of the attenuation map is probed and can be reconstructed. We have previously shown the proposed pencil-beam geometry to be feasible in imaging element maps with attenuation corrections obtained through CT transmission scans [32] or through estimation based on updated element densities [3], but it remains to be seen if accurate

Author Manuscript Author Manuscript Author Manuscript Author Manuscript

density and attenuation maps can be reconstructed without previously obtained transmission measurements.

In this work, we investigate the joint estimation of metal and attenuation maps in pencil-beam XFET, using a simplified discrete forward model and simulated data, to demonstrate the feasibility of XFET geometry and the proposed image reconstruction methods. We first investigate the conditioning of the problem with singular value decomposition (SVD) analysis of a linearized imaging model. A large condition number (i.e., the ratio of the largest to smallest singular values) indicates that the problem is ill-conditioned. An ill-conditioned matrix cannot be inverted easily and requires the use of inverse methods such as regularized iterative algorithms. To solve the inverse problem, we develop and compare two iterative image reconstruction methods to jointly estimate metal and attenuation maps: 1) a simultaneous joint estimation with conjugate gradients based on linearization, and 2) an alternating joint estimation without linearization. We performed reconstructions of metal density and attenuation maps for two numerical phantoms representing a geological iron sample and a soft tissue sample with gold. We used qualitative and normalized root mean squared error (NRMSE) comparisons to evaluate performance of the two algorithms. We present a final demonstration of the alternating approach for an $(8\ \text{cm})^3$ object containing concentrations of gold as low as 5 mg/cm^3, without knowledge of an attenuation map at any energy.

II. Methods

A. Forward model

Figures 3 and 4 display the imaging geometry of XFET. XFET can use one or more detectors; in this work, we considered a pair of opposing detectors placed on either side of the object. First, the monochromatic X-ray pencil beam of photon flux I_0 and area A_0 travels through the object with a beam attenuation map $\boldsymbol{\mu}^{(E_B)}$. Here, the discrete attenuation map vector $\boldsymbol{\mu}^{(E_B)} \in \mathbb{R}^N$, where N is the number of attenuation voxels, contains elements of linear attenuation coefficients, $\mu_k^{(E_B)}$, for each object voxel indexed by k. X-rays of energy E_B will interact with metal of density f_i, primarily through photoelectric interactions. Isotropically emitted fluorescent photons with energy E_F travel through the attenuation map at their energy, $\boldsymbol{\mu}^{(E_F)} \in \mathbb{R}^N$, and are measured at one or more opposing energy-sensitive detector planes behind central slits. The presence of the slit for a fixed pencil beam location encodes spatial information: a given column of pixels on the detector receives photons from a specific axial segment of the pencil beam of length d_0. The slit also limits the angular range for measurement and therefore limits Compton scatter contamination. For simplicity of the model, we choose d_1 to be equal to d_2, and slit width to be half the object voxel width, to allow for a 1:1 mapping between each object voxel and detector column. The object is translated perpendicularly through the fixed X-ray pencil beam to acquire data for the entire object.

The fluorescence from object voxel i measured at detector j, p_{ij}, can be modeled as

Author Manuscript Author Manuscript Author Manuscript Author Manuscript

$$p_{ij} = \frac{(d_1 + d_2)}{R_{ij}^3} I_0 A_0 D_0 d_0 s t f_i \exp\left(-\sum_k L_{ijk} \mu_k^{(E_F)}\right) \times \exp\left(-\sum_k L_{ik}^{'} \mu_k^{(E_B)}\right). \quad (1)$$

R_{ij} is the distance from the object voxel i to detector pixel j. The cubing of this distance incorporates $1/r^2$ falloff and the obliquity factor, $\frac{d_1 + d_2}{R_{ij}}$. D_0 is the area of detector pixel j. t is the exposure time, and

$$s = \frac{\tau}{\rho}(E_B)\xi_K \omega_K \nu_K \quad (2)$$

is the product of $\frac{\tau}{\rho}(E_B)$, the photoelectric cross section at the beam energy E_B; ξ_K, the probability that the photoelectric interaction will occur within the K shell; ω_K, the fluorescent yield of the K shell; and ν_K, the branching ratio of the K_α line. The factor $\exp\left(-\sum_k L_{ijk} \mu_k^{(E_F)}\right)$ describes attenuation of the fluorescent rays, where L_{ijk} denotes the intersection length of the line connecting object voxel i to detector pixel j with the pixel k. The attenuation of the X-ray beam is accounted for in the term $\left(-\sum_k L_{ik}^{'} \mu_k^{(E_B)}\right)$, where $L_{ik}^{'}$ denotes the intersection length of the line connecting the object face (where the beam is incident on the object for voxel i) and voxel i with voxel k of $\boldsymbol{\mu}^{(E_B)}$.

We can combine some known terms of (1) into a single term, $q_{ij} \equiv \frac{(d_1 + d_2)}{R_{ij}^3} I_0 A_0 D_0 d_0 s t$, which leads to the forward model

$$p_{ij} = q_{ij} f_i \exp\left(-\sum_k L_{ijk} \mu_k^{(E_F)}\right) \exp\left(-\sum_k L_{ik}^{'} \mu_k^{(E_B)}\right). \quad (3)$$

This equation represents fluorescent measurements, $\boldsymbol{p} \in \mathbb{R}^{MN}$, (where M is the number of detector pixels) in terms of the unknown metal density map $\boldsymbol{f} \in \mathbb{R}^N$ and unknown attenuation maps $\boldsymbol{\mu}^{(E_F)}$ and $\boldsymbol{\mu}^{(E_B)}$.

B. Linearization and singular value decomposition

The forward model in (1) can also be reformulated by defining two new unitless terms,

$$q_{ij}^{'} \equiv \frac{(d_1 + d_2)}{R_{ij}^3} I_0 A_0 D_0 t \exp\left(-\sum_k L_{ik}^{'} \mu_k^{(E_B)}\right), \quad (4)$$

and

$$n_i \equiv d_0 s f_i, \quad (5)$$

such that (1) becomes

Author Manuscript Author Manuscript Author Manuscript Author Manuscript

$$p_{ij} = q'_{ij} n_i \exp\left(-\sum_k L_{ijk} \mu_k^{(E_F)}\right). \tag{6}$$

Both sides of (6) can be divided by q'_{ij}, and if $n_i \neq 0 \ \forall \ i$, this new forward model can be linearized,

$$\ln\left(\frac{p_{ij}}{q'_{ij}}\right) = \ln(n_i) - \sum_k L_{ijk} \mu_k \,. \tag{7}$$

Then, defining $y_{ij} \equiv \ln\left(\frac{p_{ij}}{q'_{ij}}\right)$ and $g_i \equiv \ln(n_i)$, (7) becomes

$$y_{ij} = g_i - \sum_k L_{ijk} \mu_k \,. \tag{8}$$

In order to reexpress (8) as a matrix vector equation, we introduce data vector $\boldsymbol{y} \in \mathbb{R}^{NM}$ with elements y_m, where $m = iN + j$. Likewise, we introduce a matrix L of size $NM \times N$ with elements L_{mk}. g_i has no j dependence, so a repetition matrix R is introduced, also of size $NM \times N$,

$$R = \begin{pmatrix} \boldsymbol{r}_0 & 0 & 0 & \cdots & 0 \\ 0 & \boldsymbol{r}_0 & 0 & \cdots & 0 \\ 0 & 0 & \boldsymbol{r}_0 & \cdots & 0 \\ \vdots & \vdots & \vdots & \ddots & \vdots \\ 0 & 0 & 0 & \cdots & \boldsymbol{r}_0 \end{pmatrix}, \tag{9}$$

where $\boldsymbol{r}_0$ is a $M \times 1$ vector of ones. When $N \times 1$ vector $\boldsymbol{g}$ is multiplied by R, the resulting vector will be the same dimension as $\boldsymbol{y}$, with repeated values of $\ln(n_i)$ for every j. The vector $\boldsymbol{q}' \in \mathbb{R}^{MN}$ containing elements q'_{ij} incorporates the term L'_{ik}, which becomes extended in a similar way as $\boldsymbol{g}$. (8) can now be rewritten in matrix notation as

$$\boldsymbol{y} = R\boldsymbol{g} - L\boldsymbol{\mu}, \tag{10}$$

where $\boldsymbol{g} \in \mathbb{R}^N$ is a vector that includes linearized metal densities, and $\boldsymbol{\mu} \in \mathbb{R}^N$ is a vector of attenuation coefficients, both indexed lexicographically. To avoid scale-variance in the imaging model, we normalize L by voxel size, $L_{\max}$, and define $\boldsymbol{\mu}' \equiv \boldsymbol{\mu} L_{\max}$, such that (10) becomes

$$\boldsymbol{y} = R\boldsymbol{g} - \frac{L}{L_{\max}} \boldsymbol{\mu}' \,. \tag{11}$$

This can be written as

$$\boldsymbol{y} = A\boldsymbol{x}, \tag{12}$$

Author Manuscript Author Manuscript Author Manuscript Author Manuscript

where the block matrix $A = \left[R \mid -\frac{L}{L_{\max}}\right]$, with $A \in \mathbb{R}^{NM \times 2N}$, combines the repetition matrix and the matrix of normalized intersection lengths, and $\boldsymbol{x} \in \mathbb{R}^{2N}$ is a vector concatenating terms that contain all unknown metal densities and attenuation coefficients: $\boldsymbol{x} = \begin{bmatrix} \boldsymbol{g} \\ \boldsymbol{\mu}' \end{bmatrix}$.

To gain insight into estimability of the metal densities and attenuation map, we began our investigation of the inverse problem by performing SVD on the linearized imaging system A for a toy 5×5 object with one detector on the left-hand side of the object. Object size impacts the dimensions of A; however, the SVD of A is general for any 5×5 object (i.e., the presence of a null space revealed by the SVD will be characteristic of any object transformed by A). The decomposition $A = UD(\sqrt{\lambda})V^T$ gave the left and right singular vectors (columns of U and V, respectively) and their corresponding singular values, λ. We examined right singular vectors for patterns that indicate estimability, and singular values were plotted to examine the presence of a null space and ill-posedness. Before examination, right singular vectors corresponding to the density mapping were exponentiated, to bring them from linearized space to object space.

C. Inverse model algorithms

In the absence of attenuation, a column of detector measurements can be averaged to obtain one fluorescent measurement per object voxel, which gives a direct measurement of metal in the object without tomographic image reconstruction. The estimates from multiple detectors can be averaged to improve noise and perhaps reduce the effect of attenuation. However, this approach will underestimate the metal density of an attenuating object. Therefore, we use the mean of opposing views as a point of comparison for our more complete joint estimation algorithms, discussed in this section.

This section first considers reconstruction in the case of a known beam and fluorescent attenuation map. We then consider the case of an unknown fluorescent attenuation map and a known beam attenuation map, and finally consider a case in which neither map is known.

1) Known beam and fluorescence attenuation maps: If both the attenuation map at the beam energy and fluorescent energy are known, there is a closed-form solution for the metal densities. First, the known term q_{ij} in (3) can be combined with the known beam attenuation factor to form a new known term,

$$q''_{ij} \equiv q_{ij} \exp\left(-\sum_k L'_{ik} \mu_k^{(E_B)}\right). \tag{13}$$

(3) becomes:

$$p_{ij} = q''_{ij} f_i \exp\left(-\sum_k L_{ijk} \mu_k^{(E_F)}\right). \tag{14}$$

Assuming that p_{ij} are Poisson random variables, this model will have a Poisson likelihood function,

Author Manuscript Author Manuscript Author Manuscript Author Manuscript

$$\mathscr{L}(\boldsymbol{p};\boldsymbol{f},\boldsymbol{\mu}) = \sum_{i,j}\left\{p_{ij}\ln\left[q''_{ij}f_i\exp\left(-\sum_k L_{ijk}\mu_k\right)\right] - q''_{ij}f_i\exp\left(-\sum_k L_{ijk}\mu_k\right)\right\}, \tag{15}$$

where $\boldsymbol{\mu}$ is shorthand for $\boldsymbol{\mu}^{(E_F)}$, $\boldsymbol{f}$ is the metal density map, and $\boldsymbol{p}$ is the vector of measurements. In Appendix A, we take the derivative of the Poisson likelihood function and reveal a closed-form solution for the metal densities,

$$\hat{f}_i = \frac{\sum_j p_{ij}}{\sum_j q''_{ij}\exp(-\sum_k L_{ijk}\mu_k)}. \tag{16}$$

This result states that to obtain the maximum likelihood estimate for the metal map in (16), columns of detector pixels should be summed and divided by the column sum of their associated attenuation factors, $\exp(-\sum_k L_{ijk}\mu_k)$, multiplied by the known term q''_{ij}.

2) Known beam attenuation map, unknown fluorescence attenuation map: For the case of a known attenuation map at the beam energy, which can be obtained through previous transmission measurements, we develop and compare two iterative algorithms to jointly estimate the metal map $\boldsymbol{f}$ and the fluorescent attenuation map $\boldsymbol{\mu}$.

a) Linearized conjugate gradients approach: For the linearized imaging model developed in (12), we choose the likelihood function $\mathscr{L}(\boldsymbol{x};\boldsymbol{y})$ to be a least squares objective function, and the total objective function as

$$\begin{aligned}\phi(\boldsymbol{x};\boldsymbol{y}) &= \mathscr{L}(\boldsymbol{x};\boldsymbol{y}) + \gamma\boldsymbol{x}^T\boldsymbol{x}\\ &= (\boldsymbol{y}-A\boldsymbol{x})^T(\boldsymbol{y}-A\boldsymbol{x}) + \gamma\boldsymbol{x}^T\boldsymbol{x},\end{aligned} \tag{17}$$

where γ is the regularization parameter associated with Tikhonov regularization. Tikhonov regularization was used to aid in the reconstruction of this ill-conditioned problem. We chose to minimize this objective function with conjugate gradients. First, we constructed a vector $\boldsymbol{\Gamma} \in \mathbb{R}^{2N}$ that contained elements equal to γ, so that the regularization term could be applied to the attenuation portion of $\boldsymbol{x}$ alone. Because conjugate gradients relies on a symmetric imaging matrix and because we applied Tikhonov regularization, we define $H \equiv A^T A + \boldsymbol{\Gamma}^T I$ and $\boldsymbol{y}' \equiv A^T\boldsymbol{y}$ for use as the system matrix and data vector, respectively, in the conjugate gradients algorithm.

b) Non-linear alternating approach: The second image reconstruction method avoids linearization and alternates between updating 1) the attenuation map at the fluorescence energy with a separable paraboloidal surrogates (SPS) algorithm, and 2) the metal map with the closed form solution of (16). This alternating approach monotonically increases the objective function, which is the Poisson likelihood function with an additional quadratic roughness penalty function weighted by roughness parameter β,

Author Manuscript Author Manuscript Author Manuscript Author Manuscript

$$\phi(\mathbf{p};\mathbf{f},\boldsymbol{\mu}) = \sum_m \left\{ p_m \ln\left[q''_m f_m \exp\left(-\sum_k L_{mk}\mu_k\right)\right] - q''_m f_m \exp\left(-\sum_k L_{mk}\mu_k\right)\right\} - \beta \sum_r \frac{1}{2} w_r \left(\sum_k c_{rk}\mu_k\right)^2. \tag{18}$$

(18) uses the combined index $m = iN + j$. Remaining terms used in (18) are defined in Appendix B. The alternating approach begins with an initial estimate of the density map $\boldsymbol{f}^{(0)}$ equaling the mean of opposing views, and a constant fluorescence attenuation map $\boldsymbol{\mu}^{(0)} = 0$ for the first iteration. It also assumes a known beam attenuation map, incorporated into term q''_m. While holding the current estimate of $\boldsymbol{f}$ fixed, the attenuation map at the fluorescent energy is updated with (19), which is the SPS algorithm derived in Fessler [37] with a roughness penalty,

$$\mu_k^{(n+1)} = \left[\mu_k^{(n)} + \left(\frac{\sum_m^{N_Y} L_{mk} q''_m f_m^{(n)} \exp\left(-\sum_{k''} L_{mk''}\mu_{k''}^{(n)}\right)}{\sum_{m=1}^{N_Y} L_{mk} L_m c_m^{(n)} + \beta \sum_{r=1}^{K} |c_{rk}| c_r w_r} - \frac{\sum_m^{N_Y} L_{mk} p_m - \beta \sum_{r=1}^{K} c_{rk} w_r \sum_{k''=1}^{N} c_{k''r}\mu_{k''}^{(n)}}{\sum_{m=1}^{N_Y} L_{mk} L_m c_m^{(n)} + \beta \sum_{r=1}^{K} |c_{rk}| c_r w_r}\right)\right]_+. \tag{19}$$

The $[]_+$ enforces non-negativity. All remaining variables used in (19) are defined in Appendix B.

Holding $\boldsymbol{\mu}^{(n+1)}$ fixed, the closed-form solution found in (16) can be used to update the metal density map. Rewriting (16) for clarity with original indices i and j, the metal densities will be updated with

$$\hat{f}_i^{(n+1)} = \frac{\sum_j p_{ij}}{\sum_j q''_{ij} \exp\left(-\sum_k L_{ijk}\mu_k^{(n+1)}\right)}. \tag{20}$$

The metal density elements $\hat{f}_i$ in (20) become f_m in (19) by the index transformation $m = iN + j$. In each iteration of this algorithm, (19) and (20) are alternated.

3) Unknown beam and fluorescence attenuation maps: For an unknown beam and fluorescent attenuation map, the twostep alternating approach can still be employed for the gold object: for a pencil beam energy at the K-edge of the metal, Figure 5 shows that $\mu_k^{(E_B)}$ is related approximately to $\mu_k^{(E_F)}$ by a simple linear transformation,

$$\mu_k^{(E_B)} \approx b\mu_k^{(E_F)} + a, \tag{21}$$

for gold concentrations between 0 and 2% by weight in soft tissue. a and b are constants that are known *a priori* for a given beam energy. Using (21), $q''_m = q_m \exp\left(-\sum_k L'_{mk}\mu_k^{(E_B)}\right)$ becomes

Author Manuscript Author Manuscript Author Manuscript Author Manuscript

$$q_m'' = q_m \exp\left[-\sum_k L_{mk}'\left(b\mu_k^{(E_F)} + a\right)\right]. \tag{22}$$

When the beam attenuation map is unknown, we first assume a known density map and constant fluorescent attenuation map. Then, (19) and (20) are alternated to update the attenuation map and density map respectively, using (22) for q_m'' terms everywhere they appear (see Appendix B).

When transmission measurements are available, it is simple to acquire a beam attenuation map and use (21) to solve for a fluorescent attenuation map. However our ultimate aim is to build an algorithm that jointly estimates the metal and attenuation maps without previous knowledge of attenuation maps at any energy, to save time and dose.

D. Gold and iron phantoms

Two 20×20×20 numerical phantoms were constructed. The first was a 4 μm voxel size iron phantom with densities of 0.01, 0.70, and 1.05 g/cm^3 in a background of a carbon, oxygen, and silicon mixture, meant to represent a geological sample. The second was a 4 mm voxel size gold phantom with densities of 0.0005, 0.0050, and 0.0220 g/cm^3 in a soft tissue background, meant to resemble a biological sample similar to those used in pre-clinical imaging. Voxel sizes were chosen to maintain similar relative attenuation levels between the two phantoms, while keeping both phantoms at size $20 \times 20 \times 20$. The metal map for the gold object is shown in Figure 6; both iron and gold objects had the same shape, an adaptation of the phantom considered in Golosio et al. [14], but contained varying levels of their respective metals. The physical factors in (2) are given in Table I below for both objects.

We calculated attenuation maps for iron (6.4 keV) and gold (68.8 keV) $K_{\alpha 1}$ energies. We constructed additional attenuation maps for the K-edge energies of gold (80.7 keV) and iron (7.11 keV) to simulate attenuation maps at the pencil beam energy to account for beam attenuation. We will extend these benchtop monochromatic sources at 80.7 keV and 7.11 keV, respectively, to realistic, polychromatic sources in future work. In realistic data collection, the energy of the beam and the fluorescence X-rays are known, allowing for the linear relationship in (21) to be utilized. We assumed a Poisson noise model when simulating XFET data for these objects. Compton scatter was considered negligible due to the combination of using a monochromatic source, energy-sensitive detectors, and the limited angular range provided by the slit. However we will model Compton scatter in future investigations.

E. Simulation studies

After simulating data collection with the discrete forward model given in (1), for both iron and gold numerical phantoms, we reconstructed both objects using the linearized approach assuming a known beam attenuation map. Reconstructions with conjugate gradients used 250 iterations for both iron and gold objects, and convergence was verified by the magnitude of the gradient of the objective function, (17), reaching zero within numerical precision. The

Author Manuscript Author Manuscript Author Manuscript Author Manuscript

regularization vector $\mathbf{\Gamma}$ was nonzero only for the attenuation portion of the unknown vector in conjugate gradients, since empirically, regularization helps stabilize that estimate. We first empirically optimized γ, the elements of $\mathbf{\Gamma}$, to 1000 for both phantoms; we minimized this value while still avoiding the checkerboard effect seen when γ was too small. A vector of ones was the initial estimate for conjugate gradients for both iron and gold, and any negative values in the final attenuation map reconstructions were clipped and set to zero.

We also reconstructed iron and gold objects using the penalized alternating approach ((19) and (20)), assuming a known beam attenuation map. Iterations continued until the root mean square relative change in the density map fell below 5E–4, that is,

$$\sqrt{\frac{\sum_i \left(f_i^{(n+1)} - f_i^{(n)}\right)^2}{\sum_i \left(f_i^{(n)}\right)^2}} < 0.0005. \tag{23}$$

This criterion resulted in 20 iterations for gold and 91 iterations for iron. We first optimized β empirically to 1E–6 for iron and 1E–4 for gold. We compared the results from the alternating approach to the results from the linearized approach. The mean of opposing views was used as the initial density map estimation, and a vector of zeros was used as the initial attenuation map estimation for all alternating reconstructions. For the iron object reconstructed with the alternating approach, we also report attenuation factor maps consisting of the average attenuation factor, $\exp(-\sum_k L_{ijk}\mu_k)$, seen by all detectors for a given object voxel.

Finally, we reconstructed the gold object with the alternating approach ((19) and (20)), using the convergence criterion given in (23), assuming unknown beam and fluorescent attenuation maps. We first optimized β to 1E–4.

Additional factors in the forward model included the beam photon flux (10^{18} photons/cm^{2}s for iron, 10^{12} photons/cm^{2}s for gold), beam cross sectional area and detector pixel area (both (4 μm)^2 for iron, (4 mm)^2 for gold), exposure time (1.0 s for iron, 0.1 s for gold), fluorescence yield, probability, and other physical parameters outlined in (1). d_1 and d_2 were set to 80 μm, and slit width was 2 μm for iron. For gold, d_1 and d_2 were set to 8 cm, and slit width was 2 mm. NRMSE between reconstructed and true objects, as well as qualitative comparisons, were used to evaluate the accuracy of each method. NRMSE was defined to be the RMSE divided by the mean of the true object.

III. Results

A. SVD

Figure 7 displays a representative sample of right singular vectors corresponding to the density and attenuation maps, reshaped to object space. These singular vectors span the space of recoverable objects when the data have no noise and we use no priors. Singular values corresponding to the singular vectors are also displayed. The last 15 singular values trend downward a few orders of magnitude, indicating poor conditioning and ill-posedness, but do not reveal a null space for this discreteto-discrete model. The singular

Author Manuscript Author Manuscript Author Manuscript Author Manuscript

vectors corresponding to the largest singular values are a uniform density map coupled to attenuation pixels close to the detector. Singular vectors associated with the smallest singular values display groupings of metal density and attenuation pixels far from the detector.

B. Comparison of algorithms with known beam attenuation

Figure 8 compares reconstructions of the iron metal map for four slices of the 3D object. Slices are normal to the illumination beam's propagation direction. Included in Figure 8 is the arithmetic mean of the opposing detectors' views, without beam attenuation correction. NRMSE values calculated for each reconstruction are listed in Table II. The penalized alternating approach outperformed the linearized approach visually and quantitatively for both the iron and gold objects. The NRMSE values of the iron and gold maps estimated with the linearized approach were 196% and 438% greater, respectively, than the values obtained with the alternating approach.

Similarly, Figure 8 compares reconstructions of the attenuation map for the iron object, for four slices of the 3D object. The alternating approach visually outperformed the linearized approach, and the linearized approach resulted in NRMSE values 39% and 278% greater than those from the alternating approach for iron and gold, respectively. The linearized approach generally underestimated the attenuation maps. The attenuation maps reconstructed with both approaches are oversmoothed and are not as qualitatively accurate as the reconstructed density maps. However, the attenuation map is a nuisance parameter that serves only to enable accurate density reconstructions. So while the oversmoothing itself is not a critical issue, it could cause inaccuracies in the metal density estimate. The attenuation reconstruction with the alternating approach still provided accurate values for the average attenuation factors seen by each detector, as evident in the attenuation factor map slices in Figure 9.

C. Demonstration of alternating approach with unknown beam attenuation and noise

Figure 10 displays the density and attenuation alternating reconstructions of the gold object with an unknown beam attenuation map. The alternating approach provided accurate metal densities, resulting in NRMSE values similar to those for the alternating approach with a known beam attenuation map. The attenuation map was not as visually accurate as the density map reconstruction, but still provided NRMSE values similar to those for the alternating approach with a known beam attenuation map.

IV. Discussion and Conclusions

The SVD of the linear imaging model did not reveal a null space for this discrete-to-discrete model, indicating that we are working in a regime with estimable pixel values. However, the last 15 singular values trended downward several orders of magnitude, indicating ill-conditioning of the inverse, with particular difficulty recovering some object vectors. The singular vectors corresponding to these low values were groupings of metal pixels coupled with attenuation pixels, both far from the detector. These results indicate that metal and attenuation pixels far from the detector are least estimable and difficult to reconstruct.

Author Manuscript Author Manuscript Author Manuscript Author Manuscript

Though the SVD was performed on the linearized imaging model, any null space found would have characterized a set of indistinguishable objects in our non-linear model. Analogously, we expect from these SVD results that metal density and attenuation voxels far from the detector are difficult to reconstruct in both linear and non-linear models.

In addition to the ill-conditioning revealed by the SVD, XFET has another limitation: only attenuation voxels that lie between a point of fluorescence emission and detection will be probed and have the potential to be recovered. Therefore, the spatial distribution of metal heavily impacts what portion of the attenuation map can be recovered. We aim to systematically study this relationship in future work, and optimize detector position such that the largest portion of the attenuation map can be reconstructed. Given the SVD results and this limitation, it is straightforward to recognize the difficulty in recovering the metal and attenuation maps in XFET. Therefore, it is significant that we are able to jointly and accurately reconstruct both maps with our newly developed alternating approach.

The alternating approach outperformed the linearized approach for both the iron and gold objects, evident qualitatively in Figure 8 for the iron object and in calculated NRMSE values for both iron and gold objects. Furthermore, the attenuation estimate of the linearized approach produced non-physical negative values, which were clipped in the final step, as enforcing non-negativity with conjugate gradients is nontrivial. As previously discussed, attenuation correction is critical to obtain accurate metal maps. However exact attenuation map accuracy depicted in Figure 8 is desirable but not required: attenuation maps are nuisance parameters, serving mainly to reconstruct accurate metal density maps. As evident in the attenuation factor maps for the iron object (Figure 9), the attenuation map reconstruction still provided accurate values for the average attenuation factor seen by each detector, which is the critical piece of information needed to reconstruct accurate density maps. So while the attenuation map itself can be regarded as a nuisance parameter, its estimation heavily aids the performance of the density reconstruction.

Linearizing the model is not ideal for implementation, as one cannot take the natural log of an object containing voxels of zero metal. Taking the log transform of the data moves zeros to $-\infty$, which could be accounted for by artificially setting those values to very large negative numbers. However, this numerical manipulation destabilizes the conjugate gradients algorithm. The alternating approach does not rely on linearizing the imaging model, which is advantageous, and further emphasizes the superiority of the alternating approach for image reconstruction in pencil beam XFET.

The reasons for the alternating approach outperforming the linear approach are multi-fold. First, the two approaches assume different models: the conjugate gradients approach is linear with a least squares objective function, and the alternating approach is non-linear with a Poisson likelihood function. These inherent differences lead to a contrast in performance, especially considering the information lost with linearizing (namely, zeros in the metal density map). Second, we use different image reconstruction algorithms in each approach. In the linearized approach, we are not maximizing our knowledge of *a priori* information, as some known parameters (s and d_0) must be included in the estimated term for mathematical

Author Manuscript Author Manuscript Author Manuscript Author Manuscript

consistency. The alternating algorithm not only maximizes our knowledge of *a priori* information, but also incorporates a direct solution for half the reconstruction problem.

In this model, there is a potential for cross-talk between the metal density and attenuation map, as these variables are dependent. However, the density map reconstruction demonstrates stability in the face of error in the attenuation map, as seen by Figure 8. In our future investigations, we will study the extent of this cross-talk and its impact on the accuracy of the joint reconstruction.

We also observe that with a known beam attenuation map, most attenuation reconstructions were qualitatively more accurate towards the axial center of the objects compared to the outer slices. This is likely because ray paths pass through central object voxels more frequently than outer ones, providing more information about central voxels. The results of the SVD also support the explanation that these outer-slice voxels, which are more distant from the detector, are more difficult to reconstruct. However, if metal were placed in these outer slices, the number of X-rays passing through outer-slice voxels will increase, increasing estimability, so long as the fluorescence emitted from those voxels is not fully attenuated. Furthermore, as long as fluorescence X-rays are not fully attenuated, XFET is robust to imaging all attenuation structures, and is not limited to imaging geometrically matched attenuation and metal maps like those included here.

Using the alternating reconstruction approach on a dataset without knowledge of the beam attenuation map resulted in surprisingly accurate reconstructions. The NRMSE of the reconstructed attenuation and density maps were similar to the NRMSE values produced by the alternating approach with a known beam attenuation map. Instead of impairing the reconstruction, accounting for beam attenuation possibly provides valuable axial information about the attenuation map at the fluorescent energy, since the two attenuation maps are coupled in our formulation. By solving for the attenuation map at the beam energy in every iteration, more information was obtained about the attenuation map at the fluorescent energy, making the inverse problem better determined.

One limitation of this work was the use of a monochromatic beam and the lack of consideration of scatter. First, monochromatic beams at lower energies have been used for XFCT in benchtop settings [3], and we have previously demonstrated the functionality of this geometry with monochromatic synchroton radiation [32]. Polychromatic beams at energies necessary to cause K fluorescence in gold will be considered in future investigations, as these sources may affect our ability to reconstruct the attenuation map without any priors; this study was an introductory demonstration of the feasibility of our geometry and image reconstruction methods. Second, when using a monochromatic source, energy-sensitive detectors, and a slit with limited angular range, scatter should be minimal for our system. With the transition to polychromatic sources in future work, it will be necessary to model Compton scatter contamination to ensure its negligibility, especially for large objects. In preliminary Monte Carlo studies using a 120 kVp polychromatic source spectrum, we observe that the X-ray fluorescence signal is easily distinguished from the Compton scatter background. Additionally, in our future simulations, we intend to use mismatched voxel sizes in the forward and inverse models to better model the continuous-to-

Author Manuscript Author Manuscript Author Manuscript Author Manuscript

discrete mapping of a real system. Finally, we recognize that the beam flux used for the iron object would give prohibitive dose to the object in a medical context, however this object does not model an organism. Rather, the gold and soft tissue object is more representative of a phantom that could be used in a clinical context, and the beam flux used for this object was much lower and would likely not be dose limited. Our preliminary studies show that a beam flux an order of magnitude lower still provide accurate metal map estimates.

In summary, this work compared two image reconstruction methods: 1) a simultaneous joint estimation with conjugate gradients based on linearization, and 2) an alternating joint estimation without linearization. SVD on the linearized imaging model revealed that reconstructing metal and attenuation voxels far from the detector was an ill-conditioned problem, and that coefficients closer to the detector were less ill-conditioned and more easily recovered. Because the alternating approach outperformed the linearized approach for both iron and gold objects, and because linearizing the data posed additional problems for implementation, the alternating approach was considered superior for XFET image reconstruction. Final reconstructions with the alternating approach of a noisy $(8\ \text{cm})^3$ object containing concentrations of gold as low as $5\ \text{mg/cm}^3$ resulted in very accurate gold maps, with NRMSE values on the same order of magnitude as the model that considered a known beam attenuation map. This simulation demonstrates a successful joint reconstruction of metal and attenuation maps, using emission data only and without previous knowledge of the beam or fluorescent attenuation map.

Acknowledgment

H. A. DeBrosse would like to thank Dr. E. Sidky for his assistance in implementing the conjugate gradients algorithm. All authors declare that they have no known conflicts of interest in terms of competing financial interests or personal relationships that could have an influence or are relevant to the work reported in this paper.

This work was supported by the NIH under grant number R01EB026300, and by the AAPM/RSNA Graduate Fellowship. Partial funding for this work was provided by the NIH S10-OD025081, S10-RR021039, and P30-CA14599 awards. The contents of this paper are solely the responsibility of the authors and do not necessarily represent the official views of any of the supporting organizations. This work did not involve human subjects or animals in its research.

Appendix A

For the non-linearized imaging model, the log likelihood function is the Poisson likelihood associated with transmission tomography [37],

$$\mathscr{L}(\mathbf{p};\mathbf{f},\boldsymbol{\mu}) = \sum_{i',j}\left\{p_{i'j}\ln\left[q''_{i'j}f_{i'}\exp\left(-\sum_k L_{i'jk}\mu_k\right)\right] - q''_{i'j}f_{i'}\exp\left(-\sum_k L_{i'jk}\mu_k\right)\right\}, \tag{24}$$

where i' indexes object voxels, j indexes detector pixels, $q''_{i'j}$ are elements of the vector $\boldsymbol{q}''$, which is given by (13), and the remaining variables in (24) are defined in Appendix B. Taking the derivative of $\mathscr{L}$ with respect to the density map entries yields

$$\frac{\partial \mathscr{L}}{\partial f_i} = \sum_{i',j}\left[\frac{p_{i'j}}{f_{i'}} - q''_{i'j}\exp\left(-\sum_k L_{i'jk}\mu_k\right)\right]\frac{\partial f_{i'}}{\partial f_i}. \tag{25}$$

It is apparent that $\frac{\partial f_{i'}}{\partial f_i} = \delta_{i'i}$, so (25) becomes

$$\frac{\partial \mathscr{L}}{\partial f_i} = \sum_j\left[\frac{p_{ij}}{f_i} - q''_{ij}\exp\left(-\sum_k L_{ijk}\mu_k\right)\right]. \tag{26}$$

Setting (26) equal to zero, a closed-form solution for the density map is revealed, assuming the attenuation map is known:

$$\hat{f}_i = \frac{\sum_j p_{ij}}{\sum_j q''_{ij}\exp(-\sum_k L_{ijk}\mu_k)}. \tag{27}$$

(27) is the same as (16) and (20), which are used in the alternating approach to update the metal density map given a current guess of the attenuation map. Alternately, to maximize the Poisson likelihood in (24) for a fixed density map, the SPS algorithm can be used, which is described and derived in [37].

Appendix B

Summary of all terms in (19):

- f_m = metal density.
- p_m = detected measurements, after reindexing i and detector pixel j index into one index $m = iN + j$.
- L_{mk} = intersection lengths from the intersection of a line traveling from object pixel i to detector pixel j with the attenuation map μ_k, after consolidating detector index j and object pixel i, $m = iN + j$.
- μ_k = linear attenuation coefficient. $\mu_k^{(n)}$ is the attenuation estimation for the kth voxel on the nth iteration.
- β = scalar roughness parameter.
- c_{rk} or c_{kr} = elements of penalty matrix C, discussed further in [37]. This C only affected the attenuation map estimation.
- w_r = weights for the difference between neighboring pixels in the roughness penalty. For vertical and horizontal neighbors, $w_r = 1$, for diagonal neighbors, $w_r = 1/\sqrt{2}$, and $w_r = 0$ otherwise.

Author Manuscript Author Manuscript Author Manuscript Author Manuscript

Author Manuscript Author Manuscript Author Manuscript Author Manuscript

- $c_m^{(n)} = \begin{cases} \left[-2\frac{h(0) - h\left(l_m^{(n)}\right) + \dot{h}\left(l_m^{(n)}\right)l_m^{(n)}}{\left(l_m^{(m)}\right)^2}\right]_+ & \text{if } l_m^{(n)} \geq 0, \\ \left[-\ddot{h}\left(l_m^{(n)}\right)\right]_+ & l_m^{(n)} = 0. \end{cases}$ where h, $\dot{h}$ and $\ddot{h}$ are derivatives of the log likelihood, and given below.
- $l_m^{(n)} = \sum_k L_{mk}\mu_k^{(n)}$ is the mth line integral through the attenuation map at the nth iteration.
- $h\left(l_m^{(n)}\right) = p_m \ln\left(q_m'' f_m e^{-l_m^{(n)}}\right) - \left(q_m'' f_m e^{-l_m^{(n)}}\right)$, is the log likelihood for the mth measurement.
- $\dot{h}\left(l_m^{(n)}\right) = q_m'' f_m e^{-l_m^{(n)}} - p_m$ is the first derivative of the log likelihood.
- $\ddot{h}\left(l_m^{(n)}\right) = -q_m'' f_m e^{-l_m^{(n)}}$ is the second derivative of the log likelihood.
- $c_r = \sum_k c_{kr}$.
- $L_m = \sum_k L_{mk}$.
- N_Y = number of object-detector pixel pairs.
- $K = N \times$ number of neighbors considered in the penalty matrix C.

References

[1]. Meng LJ, Li N, and La Rivière PJ, “X-ray fluorescence emission tomography (XFET) with novel imaging geometries – a monte carlo study,” IEEE Trans. Nucl. Sci, vol. 58, no. 6, pp. 3359–3369, 2011. [PubMed: 22228913]

[2]. Manohar N, Reynoso FJ, Diagaradjane P, Krishnan S, and Cho SH, “Quantitative imaging of gold nanoparticle distribution in a tumor-bearing mouse using benchtop x-ray fluorescence computed tomography,” Sci. Rep, vol. 6, pp. 1–10, 2016. [PubMed: 28442746]

[3]. Groll A, George J, Vargas P, La Rivière PJ, and Meng LJ, “Element mapping in organic samples utilizing a benchtop x-ray fluorescence emission tomography (XFET) system,” IEEE Trans. Nucl. Sci, vol. 62, no. 5, pp. 2310–2317, 2015. [PubMed: 26705368]

[4]. Dunning CAS, and Bazalova-Carter M, “Sheet beam x-ray fluorescence computed tomography (XFCT) imaging of gold nanoparticles,” Med. Phys, vol. 45, no. 6, pp. 2572–2582, 2018. [PubMed: 29604070]

[5]. Duan X, He C, Kron SJ, and Lin W, “Nanoparticle formulations of cisplatin for cancer therapy,” WIREs Nanomed. Nanobiotechnol, vol. 8, no. 5, pp. 776–791, 2016.

[6]. Rastinehad AR, Anastos H, Wajswol E, Winoker JS, Sfakianos JP, K Doppalapudi S, Carrick MR, Knauer CJ, Taouli B, Lewis SC, Tewari AK, Schwartz JA, Canfield SE, George AK, West JL, and Halas NJ, “Gold nanoshell-localized photothermal ablation of prostate tumors in a clinical pilot device study,” PNAS, vol. 116, no. 37, pp. 18590–18596, 2019. [PubMed: 31451630]

[7]. Dorsey JF, Sun L, Joh DY, Witztum A, Zaki AA, Kao GD, Alonso-Basanta M, Avery S, Tsourkas A, Hahn SM, “Gold nanoparticles in radiation research: potential applications for imaging and radiosensitization,” Transl Cancer Res, vol. 2, no. 4, pp. 280–291, 2013. [PubMed: 25429358]

[8]. Yamada M, Foote M, and Prow TW, “Therapeutic gold, silver, and platinum nanoparticles,” WIREs Nanomed. Nanobiotechnol, vol. 7, pp. 428–445, 2015.

[9]. Dunning CAS, and Bazalova-Carter M, “Optimization of a table-top x-ray fluorescence computed tomography (XFCT) system,” Phys. Med. Biol, vol. 63, pp. 1–15, 2018.

[10]. Cheong S-K, Jones BL, Siddiqi AK, Liu F, Manohar N, and Cho SH, “X-ray fluorescence computed tomography (XFCT) imaging of gold nanoparticle-loaded objects using 110 kVp x-rays,” Phys. Med. Biol, vol. 55, pp. 647–662, 2010. [PubMed: 20071757]

Author Manuscript Author Manuscript Author Manuscript Author Manuscript

[11]. La Rivière PJ, “Approximate analytic reconstruction in x-ray fluorescence computed tomography,” Phys. Med. Biol, vol. 49, pp. 2391–2405, 2004. [PubMed: 15248585]

[12]. Di ZW, Leyffer S, and Wild SM, “Optimization-based approach for joint x-ray fluorescence and transmission tomographic inversion,” SIAM J. Imag. Sci, vol. 9, no. 1, pp. 1–23, 2016.

[13]. Schroer CG, “Reconstructing x-ray fluorescence microtomograms,” Appl. Phys. Lett, vol. 79, pp. 1912–1914, 2001.

[14]. Golosio B, Simionovici A, Somogyi A, Lemelle L, Chukalina M, and Brunetti A, “Internal elemental microanalysis combining x-ray fluorescence, Compton and transmission tomography,” J. Appl. Phys, vol. 94, pp. 145–156, 2003.

[15]. La Rivière PJ and Vargas PA, “Monotonic penalized-likelihood image reconstruction for x-ray fluorescence computed tomography,” IEEE Trans. Med. Imaging, vol. 25, no. 9, pp. 1117–1129, 2006. [PubMed: 16967798]

[16]. La Rivière PJ, Billmire DM, Vargas P, Rivers M, and Sutton SR, “Penalized-likelihood image reconstruction for x-ray fluorescence computed tomography,” Opt. Eng, vol. 45, no. 7, pp. 077005–1–077005–10, 2006.

[17]. Defrise M, Rezaei A, and Nuyts J, “Time-of-flight PET data determine the attenuation sinogram up to a constant,” Phys. Med. Biol, vol. 57, pp. 885–899, 2012. [PubMed: 22290428]

[18]. Bronnikov AV, “Approximate reconstruction of attenuation map in SPECT imaging,” IEEE Trans. Nucl. Sci, vol 42, no. 5, pp. 1483–1488, 1995.

[19]. Censor Y, Gustafson DE, Lent A, and Tuy H, “A new approach to the emission computerized tomography problem: simultaneous calculation of attenuation and activity coefficients,” IEEE Trans. Nucl. Sci, vol. NS-26, no. 2, pp. 2775–2779, 1979.

[20]. Nuyts J, Dupont P, Stroobants S, Benninck R, Mortelmans L, and Suetens P, “Simultaneous maximum a posteriori reconstruction of attenuation and activity distributions from emission sinograms,” IEEE Trans. Med. Imaging, vol. 18, no. 5, pp. 393–403, 1999. [PubMed: 10416801]

[21]. Rezaei A, Defrise M, Bal G, Michel C, Conti M, Watson C, and Nuyts J, “Simultaneous reconstruction of activity and attenuation in time-of-flight PET,” IEEE Trans. Med. Imaging, vol. 31, no. 12, pp. 2375–2382, 2012.

[22]. Natterer F, “Determination of tissue attenuation in emission tomography of optically dense media,” Inverse Probl, vol. 9, pp. 731–736, 1993.

[23]. Welch A, Clack R, Natterer F, and Gullberg GT, “Toward accurate attenuation correction in SPECT without transmission measurements,” IEEE Trans. Med. Imaging, vol. 16, no. 5, pp. 532–541, 1997. [PubMed: 9368109]

[24]. Yan Y. and Zeng GL, “Attenuation map estimation with SPECT emission data only,” Int. J. Imaging. Syst. Technol, vol. 19, no. 3, pp. 271–276, 2009. [PubMed: 20148196]

[25]. Miqueles EX and De Pierro AR, “Iterative reconstruction in x-ray fluorescence tomography based on Radon inversion,” IEEE Trans. Med. Imaging, vol. 30, no. 2, pp. 438–450, 2011. [PubMed: 20934947]

[26]. Berker Y, Keissling F, and Schulz V, “Scattered PET data for attenuation-map reconstruction in PET/MRI,” Med. Phys, vol. 41, no. 10, pp. 102502–1–2012502–13, 2014.

[27]. Brusaferri L, Bousse A, Emond EC, Brown R, Tsai Y-J, Atkinson D, Ourselin S, Watson CC, Hutton BF, Arridge S, and Theilemans K, “Joint activity and attenuation reconstruction from multiple energy window data with photopeak scatter re-estimation in non-TOF 3-D PET,” IEEE Trans. Radiat. Plasma Med. Sci, vol. 4, no. 4, pp. 410–421, 2020.

[28]. Ahn S, Cheng L, Shanbhag DD, Qian H, Kaushik SS, Jansen FP, and Wiesinger F, “Joint estimation of activity and attenuation for PET using pragmatic MR-based prior: application to clinical TOF PET/MR whole-body data for FDG and non-FDG tracers,” Phys. Med. Biol, vol. 63, pp. 1–16, 2018.

[29]. Panin VY, Aykac M, and Casey ME, “Simultaneous reconstruction of emission activity and attenuation coefficient distribution from TOF data, acquired with external transmission source,” Phys. Med. Biol, vol. 58, pp. 3649–3669, 2013. [PubMed: 23648397]

[30]. La Rivière PJ and Vargas P. “Alternating update penalized-likelihood image reconstruction for x-ray fluorescence computed tomography,” Proc. of SPIE, vol. 6318, pp. 63180Z-1 –63180Z-10, 2006.

Author Manuscript Author Manuscript Author Manuscript Author Manuscript

[31]. Shi J, Granger B, Xu K, and Yang Y, "Quantitative X-ray fluorescence imaging of gold nanoparticles using joint L1 and total variation regularized reconstruction," Quant. Imaging. Med. Surg, vol. 10, pp. 184–196, 2020. [PubMed: 31956541]

[32]. Fu G, Meng LJ, Eng P, Newville M, Vargas P. and La Rivière PJ "Experimental demonstration of novel imaging geometries for x-ray fluorescence computed tomography," Med. Phys, vol. 40, no. 6, pp. 061903–1–061903–11, 2013.

[33]. Attix FH, Introduction to radiological physics and radiation dosimetry, John Wiley & Sons, Inc., 1986.

[34]. Berger MJ, Hubbell JH, Seltzer SM, Chang J, Coursey JS, Sukumar R, Zucker DS, and Olsen K. (2010), XCOM: Photon Cross Section Database (version 1.5). [Online] Available: http://physics.nist.gov/xcom. National Institute of Standards and Technology, Gaithersburg, MD

[35]. Hubbell JH (1969), Photon cross sections, attenuation coefficients, and energy absorption coefficients From 10 keV to 100 GeV. National Standard Reference Data System.

[36]. Thompson A, Attwood D, Gullikson E, Howells M, Kim K-J, Kirz J, Kortright J, Lindau I, Liu, Pianetta P, Robinson A, Scofield J, Underwood J, Williams G, Winick H. (2009), X-ray data booklet (Third Edition), Center for X-Ray Optics and Advanced Light Source, Lawrence Berkeley National Laboratory.

[37]. Fessler JA, "Statistical image reconstruction methods for transmission tomography" in Handbook of Medical Imaging, Volume 2, Sonka M. and Fitzpatrick JM, Bellingham, Washington, USA: SPIE, 2000, ch. 1, pp. 1–70.

[38]. Hubbell JH and Seltzer SM (2004), Tables of x-ray mass attenuation coefficients and mass energy-absorption coefficients (version 1.4). [Online] Available: http://physics.nist.gov/xaamdi. National Institute of Standards and Technology, Gaithersburg, MD.

Author Manuscript

Author Manuscript

Author Manuscript

Author Manuscript

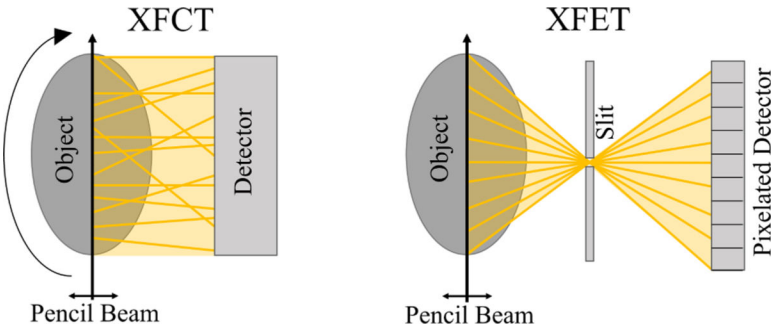

Fig. 1.
Comparison of XFCT and XFET geometry.

Author Manuscript Author Manuscript Author Manuscript Author Manuscript

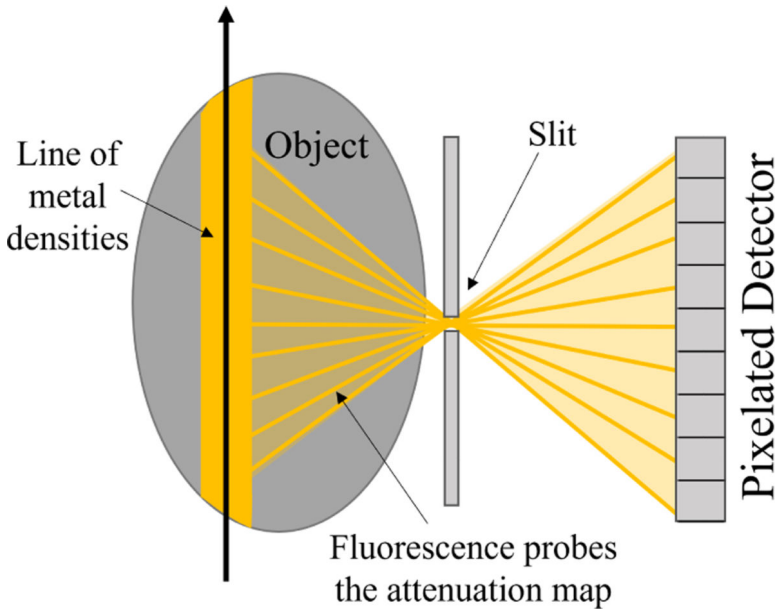

Fig. 2.

Example of an object containing a line of metal opposing the detector: measured fluorescent emissions have probed the attenuation map of the object.

Author Manuscript Author Manuscript Author Manuscript Author Manuscript

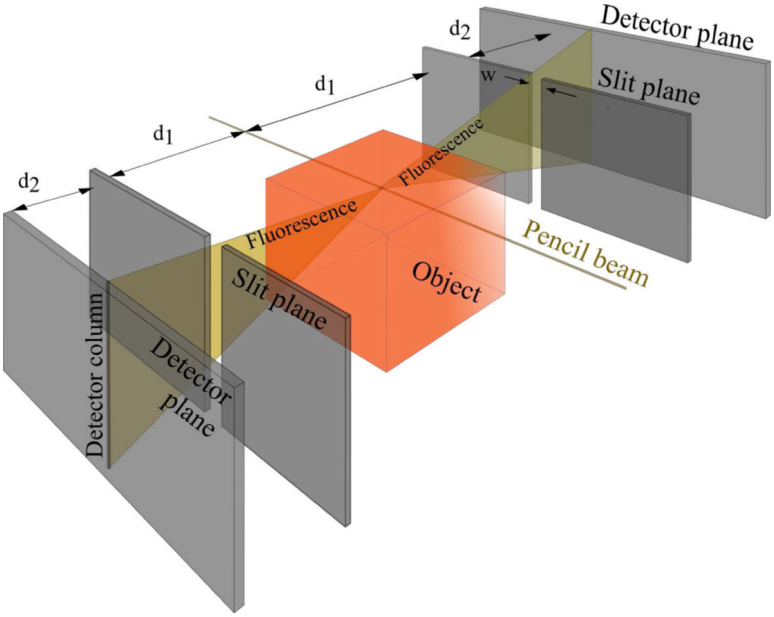

Fig. 3.

Full three-dimensional pencil beam XFET geometry used in this work, utilizing two opposing detectors.

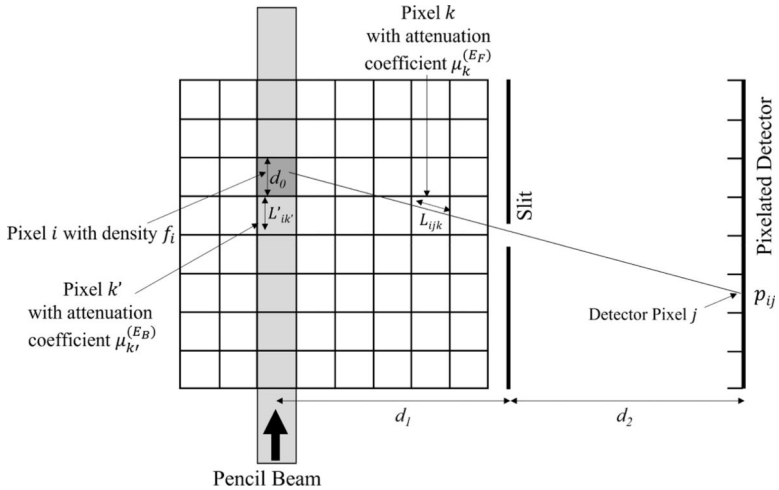

Fig. 4.

Illustration of imaging geometry, showing only one detector in two dimensions, with definition of notation. Note that the index k' is used in this figure instead of k to distinguish between attenuation at the beam energy and attenuation at the fluorescence energy.

Author Manuscript Author Manuscript Author Manuscript Author Manuscript

Author Manuscript Author Manuscript Author Manuscript Author Manuscript

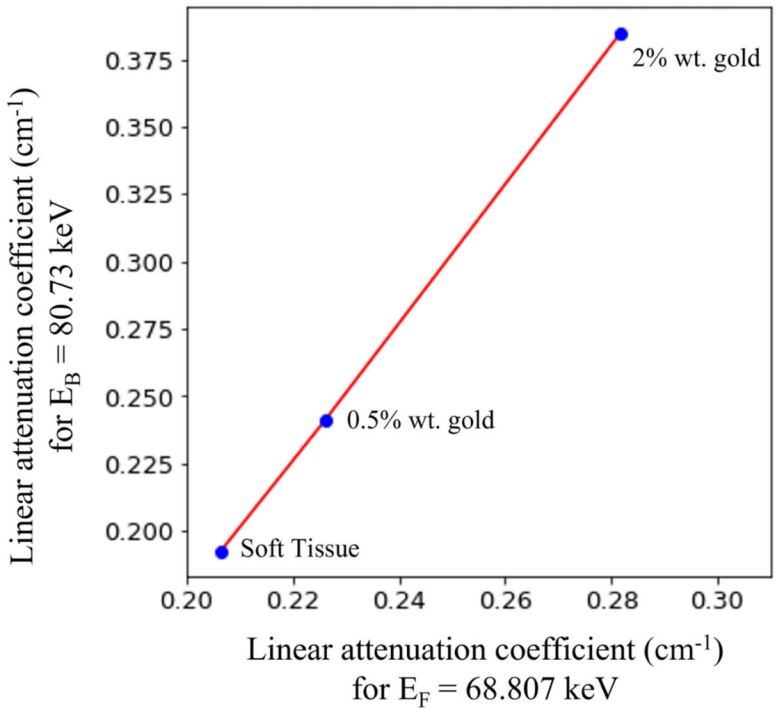

Fig. 5.

The attenuation map at the beam energy displays a linear relationship with the attenuation map at the fluorescent energy for concentrations of gold in soft tissue. The linear fit has a slope of $b = 2.5556$ and a y-intercept of $a = -0.3355$. (Data source: [38] and [33]).

Author Manuscript Author Manuscript Author Manuscript Author Manuscript

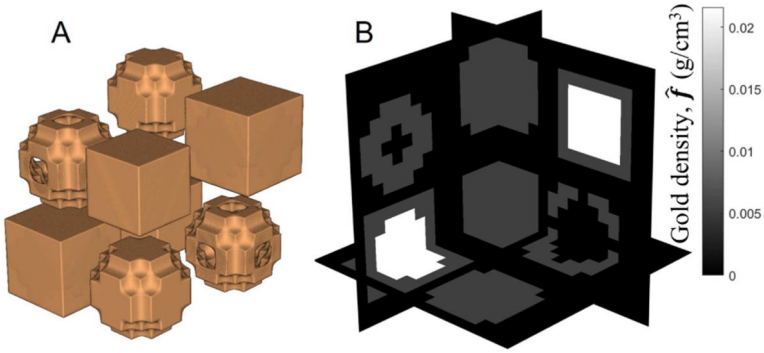

Fig. 6.

Gold object. A) volumetric view of gold densities, B) slices of gold density object showing buried regions of dense gold. The attenuation map is not shown, but resembles the shape of this object and includes a cubic soft tissue background.

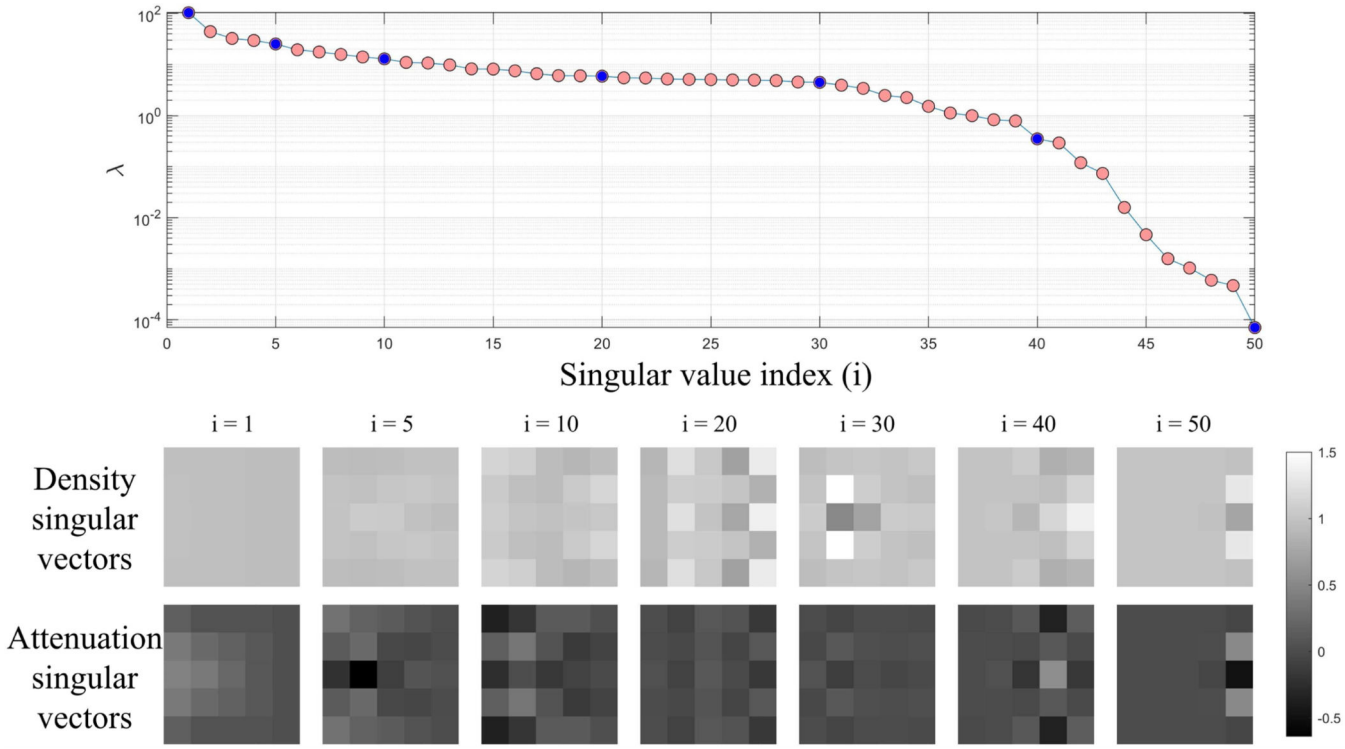

Fig. 7.

Right singular vectors of the system matrix A for the left detector, corresponding to the density map and attenuation map, reshaped in object space. Top: Eigenvalues corresponding to the displayed singular vectors.

Author Manuscript Author Manuscript Author Manuscript Author Manuscript

Author Manuscript Author Manuscript Author Manuscript Author Manuscript

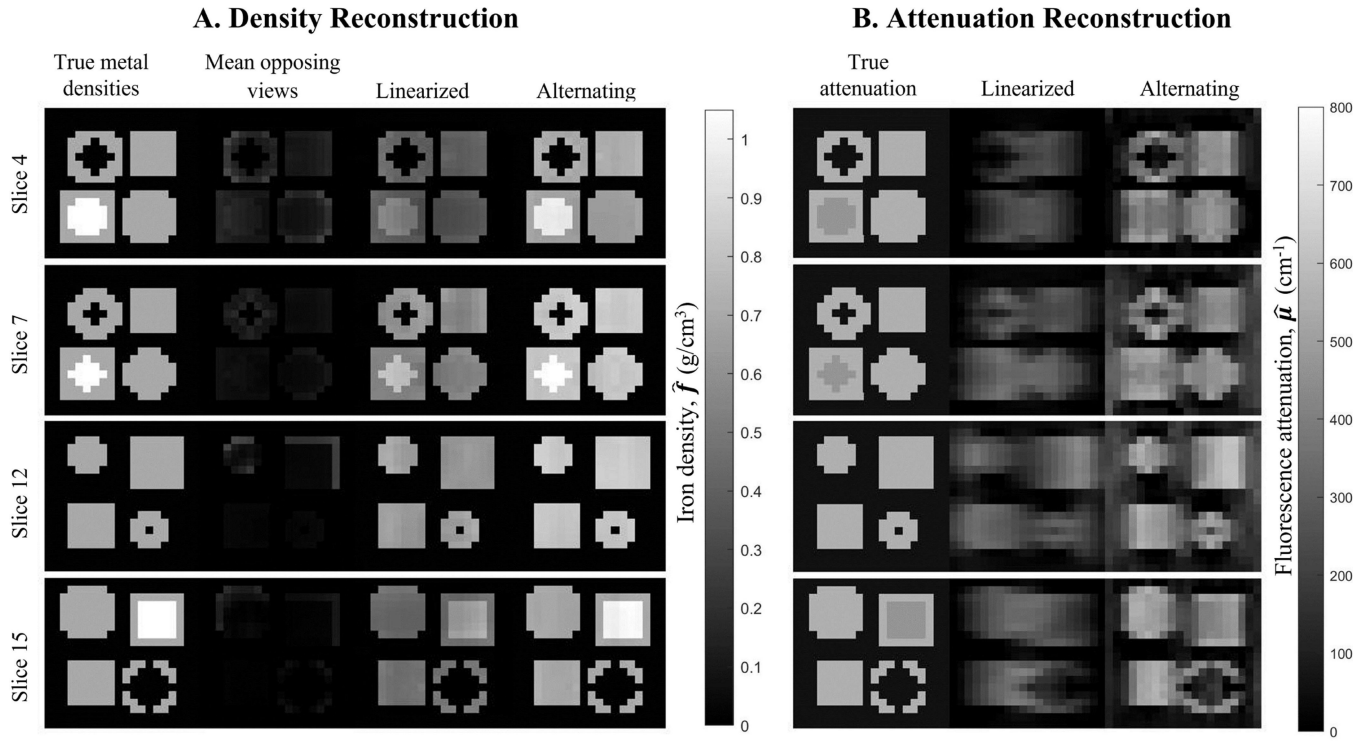

Fig. 8.

A). Slices through reconstructed density maps and true iron object. From left to right: true density map, mean of opposing views without attenuation correction, linearized approach (250 iterations, $\lambda = 1000$), alternating approach (penalized, 91 iterations, $\beta = 1\text{E} - 6$). B). Slices through reconstructed iron attenuation maps and true attenuation map. From left to right: true attenuation map, linearized approach, alternating approach. From top to bottom: slice 4 of 20, slice 7 of 20, slice 12 of 20, slice 15 of 20.

Author Manuscript Author Manuscript Author Manuscript Author Manuscript

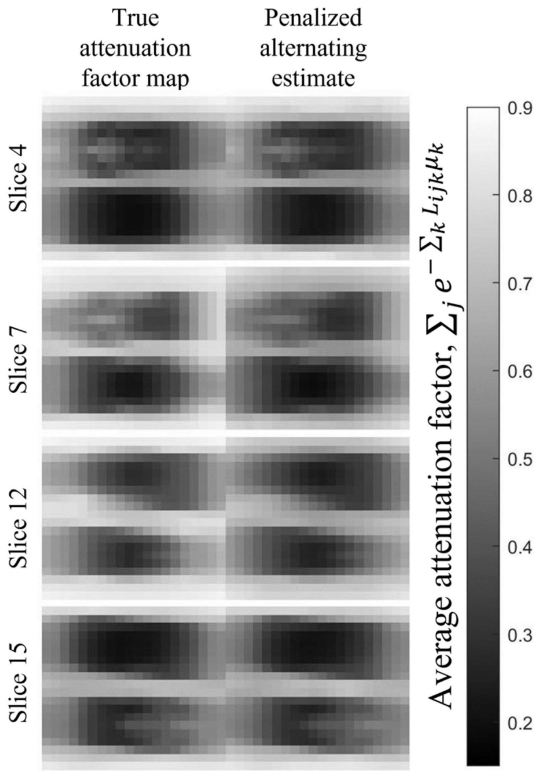

Fig. 9.

Slices through true and estimated average attenuation factor maps. Each displayed voxel contains the average attenuation factor, $\exp(-\sum_k L_{ijk}\mu_k)$, seen by every detector for that emission voxel. Reconstructions were completed with the penalized alternating approach ($\beta = 1\text{E}-6$, 91 iterations). From top to bottom: slice 4 of 20, slice 7 of 20, slice 12 of 20, slice 15 of 20.

Author Manuscript Author Manuscript Author Manuscript Author Manuscript

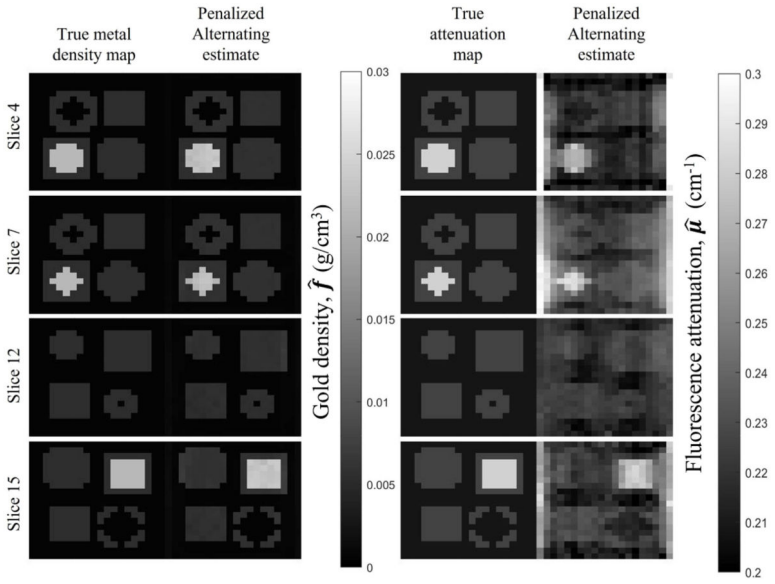

Fig. 10.

Left: Slices through reconstructed gold metal maps and true metal maps. Right: slices through reconstructed and true attenuation maps. All reconstructions were completed with the penalized alternating approach ($\beta = 1\text{E} - 4$, 78 iterations). From top to bottom: slice 4 of 20, slice 7 of 20, slice 12 of 20, slice 15 of 20.

Author Manuscript

Author Manuscript

Author Manuscript

Author Manuscript

TABLE I

PHYSICAL FACTORS OF (2) FOR IRON AND GOLD OBJECTS

	Iron	Gold
$\frac{\tau}{\rho}(E_B)\left[cm^2/g\right]$	405.9	8.5
ξ_K	0.88	0.82
w_K	0.36	0.96
v_K	0.60	0.50

Data were taken from [33], [34], [35], and [36]

Author Manuscript Author Manuscript Author Manuscript Author Manuscript

TABLE II

NRMSE VALUES FOR IRON AND GOLD DENSITY AND ATTENUATION MAPS, FOR COMPARED RECONSTRUCTION METHODS

Object	NRMSE	
	Linearized	*Alternating*
Iron model, known beam attenuation		
Density Map	0.77	0.26
Attenuation Map	1.04	0.75
Gold model, known beam attenuation		
Density Map	0.70	0.13
Attenuation Map	0.68	0.18
Gold object, unknown beam attenuation		
Density Map	-[a]	0.19
Attenuation Map	-[a]	0.14

[a]Dashes indicate reconstructions not explored.